



# CH PLIF and PIV implementation using C-X (0,0) and intra-vibrational band filtered detection

Stephen D. Hammack<sup>1</sup> · Aaron W. Skiba<sup>2</sup> · Tonghun Lee<sup>3</sup> · Campbell D. Carter<sup>1</sup>

Received: 22 August 2017 / Accepted: 16 December 2017 / Published online: 3 February 2018

© This is a U.S. Government work and not under copyright protection in the US; foreign copyright protection may apply 2018

## Abstract

This study demonstrates advancement in a low-pulse energy methylidyne (CH) planar laser-induced fluorescence (PLIF) method that facilitates its application alongside flows seeded for particle image velocimetry (PIV) or other particle scattering based methods, as well as in high scattering environments. The C-X (0,0) R-branch excitation and filtered detection are carefully selected such that the laser line frequency is heavily attenuated by an edge filter while allowing transmission of most of the (0,0) band fluorescence. There are strong OH A-X (0,0) lines in the vicinity, but they can be avoided or utilized through dye laser tuning. As a demonstration of efficacy, PIV is performed simultaneously with the PLIF imaging. Using the edge filter, particle scattering signal is reduced to sub-fluorescence levels, allowing for flame-front analysis. This achievement enables flame-front tracking at high repetition rates (due to the low-pulse energy required) in combination with a scattering method such as PIV or use in high scattering environments such as enclosed combustors or near burner surfaces.

## 1 Introduction

Planar laser-induced fluorescence of combustion radicals for the purpose of flame observation is a well-established and non-invasive diagnostic. Imaging of the hydroxyl (OH) radical, paired with particle image velocimetry (PIV), is an effective technique, in large part due to the ability to filter out particle scattering signal while obtaining strong fluorescence using an OH A-X (1,0) excitation while detecting only the (0,0) and (1,1) fluorescence. The methylidyne (CH) radical is an excellent flame marker, because of its rapid production and consumption on either side of the high-temperature reaction surfaces, and therefore good correlation with heat release [1], but low number density has limited CH PLIF applications. Still, simultaneous CH PLIF—employing B-X (0,0) excitation and A-X detection—and PIV has been demonstrated as a tool to characterize flame-front topology with individual snapshots [2–5]. More recent efforts have sought

to temporally resolve CH PLIF measurements using either an Alexandrite laser [6] or an optical parametric oscillator (OPO) pumped by a custom Nd:YAG burst laser [7, 8]. The combination of 10-kHz CH PLIF and PIV has now been implemented with the use of a diode-pumped solid-state (DPSS) Nd:YAG/dye laser system for CH radical excitation [9], wherein the B-X/A-X excitation/detection scheme was employed, which required use of the frequency-tripled output of the Nd:YAG laser and a short-lived *blue* (exciton exalite) laser dye.

In 2014, Carter et al. demonstrated the efficacy of utilizing the C-X (0,0) band for CH [10] and CH–OH PLIF [11]. This approach has advantages over contemporary excitation methods of greater Einstein coefficients and an excitation wavelength ( $\lambda_{\text{ex}} = 310\text{--}320\text{ nm}$ ) accessible to frequency-doubled dye lasers using efficient and long-lived red dyes. Aside from facilitating high-quality CH PLIF imaging, the transition strength and line position make a C-X excitation well suited for high-repetition-rate (kHz) acquisitions. There have been three perceived disadvantages to the C-X excitation: (1) the proximity to the OH A-X (1,1) and (0,0) bands, (2) signal loss to predissociation of the upper state, and (3) the need to use resonant detection due to the absence of strong diagonal transitions in the C-X system.

In the introduction of the technique, it was shown that Nd:YAG/dye laser systems, both a “traditional” 10-Hz and

✉ Stephen D. Hammack  
stevehammack@gmail.com

<sup>1</sup> Air Force Research Laboratory, Wright-Patterson AFB, OH 45433, USA

<sup>2</sup> Department of Aerospace Engineering, University of Michigan, Ann Arbor, MI 48109, USA

<sup>3</sup> Department of Mechanical Science and Engineering, University of Illinois, Urbana, IL 61801, USA

a 10-kHz DPSS setup, have sufficiently narrow linewidth to resolve and isolate CH and OH lines in the region, addressing issue (1). Furthermore, initial imaging and follow-up turbulent flame applications have demonstrated that (2) predissociation does not preclude high fluorescence signal collection, and that (3) laser line surface scattering does not necessarily preclude application for an open-flame measurement. However, these successful demonstrations have addressed neither the challenges nor solutions for dealing with strong particle scattering, as would be encountered in a PIV (particle image velocimetry) measurement, nor the scattering inherent to enclosed combustor applications. A solution, first suggested by Carter et al. [11], lies in shifting the excitation transition from near the Q-branch bandhead, as previously used, to a transition of the R-branch. With the excitation wavelength located away from the center of the electronic band, a long-wave-pass filter could reject the laser scattering while still transmitting the Q- and P-branch emission with very little attenuation, provided the edge is sufficiently steep and properly placed. Furthermore, the  $R_1$  and  $R_2$  spin-split pairs are well overlapped in the  $J=11$  to  $J=13$  range [12]. This publication demonstrates the efficacy of such an approach by sharing experimental results of CH PLIF in a piloted-Bunsen burner using the C-X (0,0) R(13) or R(11) excitation lines and a steep-edged, long-wave-pass filter for intra-vibrational band filtering our fluorescence detection.

## 2 Setup

This experiment utilized six primary components: (1) an Nd:YAG and (2) a frequency-doubled dye laser system to produce the excitation beam and (3) the intensified charge-coupled device (ICCD) camera for fluorescence detection; (4) a dual-cavity Nd:YAG for the PIV scattering beam and (5) an interline-transfer CCD camera for PIV scattering detection; and (6) the piloted and premixed Bunsen burner. These components were suitable to achieve the goal of demonstrating the effectiveness of the novel filtering method and the ability to collect high fidelity data for turbulent flames. Figure 1 illustrates the equipment layout.

### 2.1 PLIF

A frequency-doubled Nd:YAG laser (Quanta-Ray GCR170) pumped a dye laser (Lumonics HD-300) containing DCM dye (Exciton) in methanol at a 10-Hz repetition rate. The 622-nm dye laser output passed through frequency-doubling and wavelength separation units (Inrad Autotracker III) to produce 311-nm radiation. Beam shaping optics included a telescope, a rectangular concave lens for vertical divergence, and a spherical lens for vertical

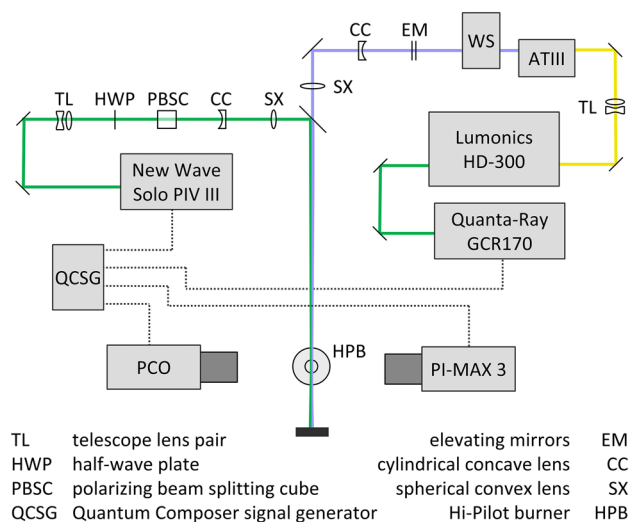


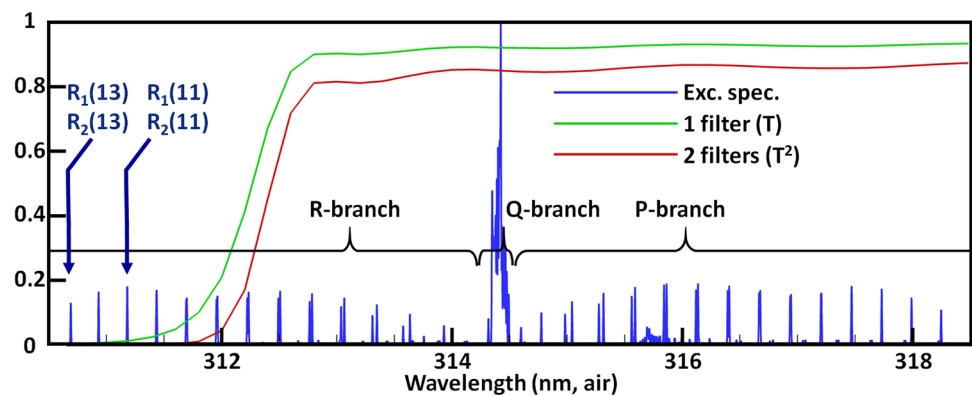
Fig. 1 A diagram of the experiment setup

collimation as well as horizontal focusing to produce a narrow waist through the probe region. The resulting sheet was approximately 50-mm tall and approximately 0.17-mm wide (FWHM). The pulse energy, obtained at the dye laser exit, was near 1 mJ. Losses due to optics and clipped edges of the well expanded sheet are estimated to be roughly 50% based on measurements of laser power post optics in previous/similar setups.

The excitation and detection method makes use of the wavelength separation between the rotational branches of the C-X (0,0) band. To facilitate intra-vibrational band filtering, the excitation line is chosen from the R-branch with a high rotational number. A long-wave-pass edge filter with a steep slope can be used to strongly attenuate emission below 311 nm and still transmit most of the Q- and P-branch fluorescence. The overlapped  $R_1(13)$  and  $R_2(13)$  lines ( $\lambda_{ex} = 310.690$  nm, in air) are sufficiently strong and isolated from the band center (314–315 nm) for effective filtering. The  $R_1(11)$  and  $R_2(11)$  transitions ( $\lambda_{ex} = 311.180$  nm, in air) are even stronger but are also closer to the band center. In this pursuit, a custom filter has been designed and produced in a small quantity by Semrock, Inc. (AFRL-0002) (Fig. 2).

Fluorescence was collected using an ICCD camera (Roper Scientific PI-MAX 3 Superblue) equipped with an  $f/2.8$  100-mm UV lens (Sodern Cerco). In the PLIF images presented in this paper, a combination of two AFRL-0002 filters (to improve rejection) and one UG5 Schott glass filter were used, and the  $R_1(11)$  and  $R_2(11)$  lines were chosen for excitation. The field-of-view was determined by imaging a ruled target and found to be  $47 \times 47$  mm<sup>2</sup>. Binning reduced the  $1024 \times 1024$  pixel array to  $512 \times 512$  pixels, yielding a digital resolution of 92  $\mu$ m per pixel. The intensifier was

**Fig. 2** An excitation spectrum of the CH C-X (0,0) band computed using LIFBASE [13] at a temperature of 1600 K. Curves are plotted for the transmission function  $T$  (manufacturer provided, actual) of the AFRL-0002 filter. In practice, two filters were used and so the transmission function is  $T^2$ . Two candidates for R-branch excitation are marked to the far left



gated to 100 ns, and the fluorescence was temporally centered within the gate.

## 2.2 PIV

A dual-cavity frequency-doubled Nd:YAG laser (New-Wave Solo PIV) provides two 532-nm pulses separated by  $\Delta t = 4 \mu\text{s}$ . Pulse energy was manipulated by adjusting flash-lamp energy and Q-switch delay so as to provide similar energy in each pulse, about 20 mJ, while a halfwave plate and polarizing cube acted as an attenuator on both pulses. Beam-shaping optics expanded the beam into a laser sheet before a final mirror combined it with the 311-nm sheet. Particle scattering was imaged using an interline-transfer charge-coupled device (CCD) camera (PCO 1600) positioned on its side such that the image is taller, 1600 pixels, than it is wide, 1200 pixels. The field-of-view is 38 mm wide and 50 mm tall, with a  $31 \mu\text{m}$ -per-pixel digital resolution. The image pairs were processed into velocity vector fields using DaVis 8.4 (LaVision). Interrogation regions were 50% overlapping  $16 \times 16$  pixel windows for the first four passes, then decreasing to a minimum size of  $8 \times 8$  for the final four passes.

## 2.3 Burner

The high-turbulence Hi-Pilot II burner was used for this demonstration. The 21.6-mm (ID) central tube issued a premixed flow of 454 SLPM air and 50.1 SLPM  $\text{CH}_4$ , an equivalence ratio of  $\phi = 1.05$ , at a mean centerline velocity of 32 m/s with a turbulent Reynolds number of  $\text{Re}_T = 7900$  and a turbulence intensity (normalized by the laminar flame speed) of  $u'/S_L = 25.9$ . A large-area annular pilot flame, with a 130-mm diameter, provides a co-flow, with a total premixed flow rate of 476 SLPM, at near stoichiometric composition ( $\phi = 0.98$ ). The co-flow burns close to the expanded steel cap, positioned below the main flow exit, such that it provides an annulus of hot products around the central jet flow. The central flow was seeded from a fluidized bed

of 150–250 nm (agglomerated)  $\text{TiO}_2$  particles (LaVision 1108953). The burner position was adjusted using an XYZ translation stage while the cameras remained static. More detailed discussion of the Hi-Pilot burner and the “Case 3A” flame conditions used here can be found in Refs. [14, 15].

## 2.4 Acquisition control and timing

A signal generator (quantum composer) was used as a master timing device for synchronization, with camera signals gated by an acquisition input (Stanford Research Systems). Camera gating and laser timing were observed using camera monitor ports and photodiode signals on an oscilloscope for confirmation. The lasers were timed such that the PLIF pulse occurred  $1 \mu\text{s}$  after the first PIV pulse for all cases. Glass and aluminum targets were imaged for registration and field-of-view (FOV) measurement, with illumination from a UV LED for the PLIF camera.

## 3 Results and discussion

### 3.1 CH PLIF and PIV

The application of a C-X excitation strategy with a seeded flow is shared in Fig. 3. The combination of filters proved to be very effective; no significant particle scattering, Rayleigh scattering, or OH LIF were observed. Initially, the R(11) lines were passed over in favor of the slightly weaker R(13) transitions in an effort to increase the wavelength distance between the laser line and filter edge. However, we did not experience any interference from scattering when we adjusted from R(13) to R(11) lines. Note that the R(12) lines overlap with the OH A-X (0,0)  $Q_1(13)$  line to such a degree that it is not possible to bias towards the CH peak over the OH peak; furthermore, the OH fluorescence is many times stronger, and so the CH R(12) lines are not suitable. Note-worthy too is the relative contribution of A-X and B-X fluorescence via electronic energy transfer; this was estimated

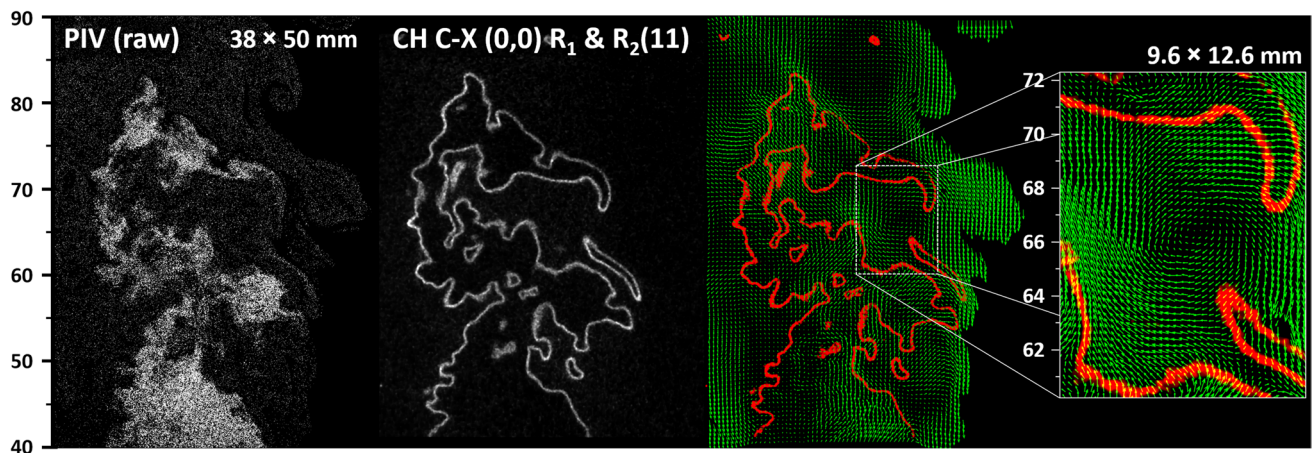


**Fig. 3** An example of simultaneous CH PLIF and PIV using the CH C-X (0,0)  $R_1$  and  $R_2(11)$  lines near 311.180 nm. One of the PIV camera images shows the scattering from seed particles (left) alongside a CH PLIF image after background subtraction and projective mapping (center left). The computed velocity vector field is overlaid at 1/16th

density onto the CH PLIF image, with green arrows for velocity and red coloring for the CH signal (center right). A denser velocity field, where one vector is plotted for every four vectors calculated, is shown over an enlarged region (right). The downstream location (in mm) is marked by the vertical scales

to be two orders of magnitude weaker than the C-X fluorescence using different filters to compare emission of the different bands.

The signal-to-noise (SNR) ratio has been estimated using 10 OH PLIF images acquired with all parameters but excitation wavelength held constant. This allows one to calculate an interrogation region ( $12 \times 12$  pixels) with the assumption that the true signal should be constant and that all variance is noise, producing a conservative lower bound on SNR. The OH PLIF images were first processed by subtracting an average image of flame background signal to avoid improperly counting chemiluminescence as signal, and flat-field corrected. To account for the higher mean OH signal than found in the CH PLIF images and therefore lower shot noise, the OH image SNR values are multiplied by the square root of the ratio of CH to mean OH signal. In this way, we have estimated the SNR to be  $> 6.5$  with respect to the mean CH signal along the flame-front curve, and with  $\text{SNR} \approx 10$  with respect to peak CH signals; SNR values increase further with some filtering (e.g., median filtering) of the image. The background due to any OH A-X fluorescence, sampled from the product region near the flame in the data, is  $\sim 5\%$  of CH signal. Any background signal caused by particle scattering is indistinguishable from other background sources in the PLIF images. Measurements in lean flames, where CH number densities are expected to be lower, have been examined in the same manner, with the SNR in  $\varphi = 0.85$  flames found to be just over half the value for the  $\varphi = 1.05$ ; one can expect  $> 3.4$  for mean CH signal and  $> 5$  for peak signal segments. The particle seeding density is sufficiently great

for production of a high-resolution velocity vector grid (i.e.,  $\sim 0.25$  mm for final interrogation window).

### 3.2 OH PLIF and PIV

The presence of strong OH A-X lines in the region is an obstacle to avoid for pure CH excitation, but it also makes OH PLIF accessible with a small dye laser wavelength adjustment. We made use of an isolated nearby OH A-X (0,0) transition, the  $Q_1(12)$  line, at a wavelength of 310.602 nm. Signal detection still makes use of resonant rejection by the filter(s). Signals are nearly five times that of the CH images. Figure 4 contains an example of data collected after adjusting the dye laser to excite OH. Unfortunately, there does not seem to be CH and OH transitions with a fortuitous spacing to facilitate combined CH–OH PLIF imaging.

These measurements were undertaken as a proof of concept, and thus in-depth analysis of the Hi-Pilot flames was beyond the scope of the work. Nonetheless, it is clear that the approach allows tracking of eddies (at very high resolution) in relation to the flame-front location as well as the derivation of statistical information (e.g.,  $u'$ ,  $v'$ , etc.) conditioned on the reaction layers themselves. Greater understanding of preheat-zone broadening and its effect on turbulent flame propagation, may also be afforded by the new technique (see Ref. [16]). Moreover, based on the results here, it appears possible that the measurement technique can be extended to the kHz domain, which would allow tracking of eddies and flame-front movement in real time.

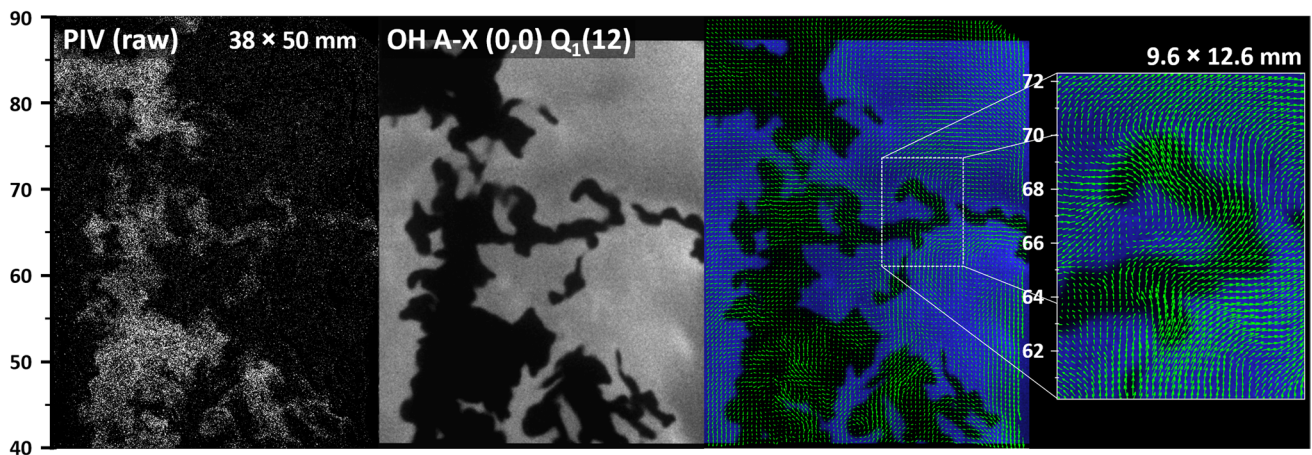


**Fig. 4** An example of simultaneous OH PLIF and PIV performed using a nearby OH A-X (0,0) transition near 310.602 nm. One of the PIV camera images shows the scattering from seed particles (left) alongside an OH PLIF image after background subtraction and projective mapping (center left). The computed velocity vec-

tor field is overlaid at 1/16th density onto the OH PLIF image, with green arrows for velocity and red coloring for the OH signal (center right). A denser velocity field, where one vector is plotted for every four vectors calculated, is shown over an enlarged region (right). The downstream location (in mm) is marked by the vertical scales

**Acknowledgements** The authors of this work would like to thank the AFOSR and the High Speed Systems Division, Aerospace Systems Directorate (AFRL/RQ), for their support in these efforts. Stephen D. Hammack held an NRC Research Associateship at Wright-Patterson AFB while performing this research.

## References

1. C.M. Vagelopoulos, J.H. Frank, *Proc. Combust. Inst.* **30**, 241 (2005)
2. C.D. Carter, J.M. Donbar, J.F. Driscoll, *Appl. Phys. B* **66**, 129 (1998)
3. D. Han, M. Mungal, *Proc. Combust. Inst.* **28**, 261 (2000)
4. P. Kothnur, M. Tsurikov, N. Clemens, J. Donbar, C. Carter, *Proc. Combust. Inst.* **29**, 1921 (2002)
5. M. Tanahashi, S. Murakami, G.-M. Choi, Y. Fukuchi, T. Miyauchi, *Proc. Combust. Inst.* **30**, 1665 (2005)
6. Z. Li, J. Kiefer, J. Zetterberg, M. Linvin, A. Leipertz, X. Bai, M. Aldén, *Proc. Combust. Inst.* **31**, 727 (2007)
7. N. Jiang, R.A. Patton, W.R. Lempert, J.A. Sutton, *Proc. Combust. Inst.* **33**, 767 (2011)
8. J.D. Miller, S.R. Engel, T.R. Meyer, T. Seeger, A. Leipertz, *Opt. Lett.* **36**, 3927 (2011)
9. A. Johchi, Y. Naka, M. Shimura, M. Tanahashi, T. Miyauchi, *Proc. Combust. Inst.* **35**, 3663 (2015)
10. C.D. Carter, S. Hammack, T. Lee, *Appl. Phys. B* **116**, 515 (2014)
11. C.D. Carter, S. Hammack, T. Lee, *Combust. Flame* **168**, 66 (2016)
12. J.B. Jeffries, R.A. Copeland, D.R. Crosley, *J. Quant. Spec. Rad. Trans.* **37**, 419 (1987)
13. J. Luque, D.R. Crosley, LIFBASE: Database and Spectral Simulation Program (Version 1.5) SRI International Report MP, 99-009 (1999)
14. A.W. Skiba, T.M. Wabel, C.D. Carter, S.D. Hammack, J.E. Temme, T. Lee, J.F. Driscoll, *Proc. Combust. Inst.* **36**, 4593 (2017)
15. A.W. Skiba, T.M. Wabel, C.D. Carter, S.D. Hammack, J.E. Temme, J.F. Driscoll, *Combust. Flame* (2017). <https://doi.org/10.1016/j.combustflame.2017.08.016>
16. A.W. Skiba, C.D. Carter, S.D. Hammack, T. Lee, *Combust. Flame* **189**, 207 (2018)